Correlations in ion channel expression emerge from homeostatic tuning rules

Timothy O'Leary, Alex H Williams, Jonathan S Caplan and Eve Marder

Affiliations

All authors: Volen Center for Complex Systems, Brandeis University, Waltham MA, 02454, USA.

Corresponding author

Eve Marder (marder@brandeis.edu)

Author contributions

TO and EM conceived the study; TO developed theory; TO, AHW and JSC designed and performed simulations; TO prepared the figures; TO and EM wrote the manuscript. All authors read and approved the final manuscript.

Funding

NIH grant MH 46742

Abstract

Experimental observations reveal that the expression levels of different ion channels vary dramatically across neurons of a defined type, even when these neurons exhibit stereotyped electrical properties. However, there are robust correlations between different ion channel expression levels, although the mechanisms that determine these correlations are unknown. Using generic model neurons we show that correlated conductance expression can emerge from simple homeostatic control mechanisms that couple expression rates of individual conductances to cellular readouts of activity. The correlations depend on the relative rates of expression of different conductances. Furthermore, we show that homeostatic regulation is remarkably insensitive to the details that couple the regulation of a given conductance to overall neuronal activity because of degeneracy in the function of multiple conductances and can be robust to 'anti-homeostatic' regulation of a subset of conductances expressed in a cell.

Significance statement

Neurons develop and maintain their electrical properties according to homeostatic rules that ensure robustness to perturbations and channel turnover. It is not currently understood how such homeostatic regulation rules shape the long term expression of ion channel types in specific neuron classes nor how finely-tuned these rules need to be. We show that generic activity-dependent regulation rules constrain the distribution of different membrane conductances to reveal correlations in their relative densities, as has been recently observed experimentally. Specific correlations in ion channel expression to depend on expression rates, and the regulation rules themselves are far more robust than previously thought.

Introduction

The electrophysiological signature of each neuron is determined by the number and kind of voltage-dependent conductances in its membrane. Most neurons express many voltage-dependent conductances, some of which may have overlapping, or degenerate physiological functions (1-5). Furthermore, neurons in the brains of long-lived animals must maintain reliable function over the animal's lifetime while all of their ion channels and receptors are replaced in the membrane over hours, days or weeks. Consequently, ongoing turnover of ion channels of various types must occur without compromising the essential excitability properties of the neuron (5-9).

Both theoretical and experimental studies suggest that maintaining stable intrinsic excitability is accomplished via homeostatic, negative feedback processes that use intracellular Ca^{2+} concentrations as a sensor of activity, and then alter the synthesis, insertion, degradation of membrane conductances to achieve a target activity level (10-26). Among the modeling studies are several different homeostatic tuning rules that differ in how sensor read-out is coupled to the changes in conductance necessary to achieve a target activity (10, 12, 13, 27). Regardless, these models can self-assemble from randomized initial conditions, and they will change their conductance densities in response to perturbation or synaptic drive. In one of these homeostatic self-tuning models (13), similar activity patterns can be associated with different sets of conductance densities.

Thus, it is perhaps not surprising that experimental studies also find a considerable range in the conductance densities of voltage-dependent channels and in the mRNA expression of their ion channel genes (28-35). The experimental studies also showed clear correlations in these expression patterns (29, 31-34). It is therefore possible that these correlations are crucial for the electrophysiological behavior of the neuron in question. However, when large numbers of model neurons (without a homeostatic tuning rule) were made from random sets of conductance parameters and then searched for those that produce a specific behavior, they did not show correlations in conductance expression that resemble the experimental findings (36). This raised the question of how the correlations seen in the experimental data are established and

whether they are somehow genetically hard-wired. For example, correlations in ion channel expression may simply result from explicit co-regulation, such as control of gene expression by a common transcription factor or silencing of a subset of genes in a certain population of cells. Another possibility is that correlations emerge from some interaction between activity-dependent regulatory processes that control the expression of different ion channel types.

We address this question in this paper using theory and computational models. We show that correlations in ion channel expression emerge as a consequence of homeostatic control mechanisms that couple the expression rates of individual conductances to a cell-intrinsic readout of activity. Importantly, the shape of the correlation pattern is determined by the relative rates of expression of different conductances. Furthermore, we show how degeneracy implies that regulatory control mechanisms do not need to be as precisely tuned as previously anticipated. For example, subsets of conductances can be regulated anti-homeostatically without interfering with convergence to a target activity level. Thus, there is considerable flexibility in how different conductances can be regulated while maintaining a 'set-point' in activity. This flexibility is compatible with distinct correlation patterns seen in the conductance expression of different neuron types.

Results

There are several existing homeostatic neuron models that use intracellular Ca^{2+} concentrations to regulate their conductances (10, 12, 13, 17, 27, 37). These models are capable of producing and maintaining complex activity patterns such as rhythmic bursting that rely on the interactions between many voltage-dependent conductances and Ca^{2+} dynamics. Analysis of these models is often mathematically intractable and it is also difficult to develop an intuitive understanding of how the distribution of conductances is shaped over time. Therefore, in this study we start with a toy model with three non-voltage-dependent conductances and simple Ca^{2+} dynamics. We then progress to a more complicated spiking model with three regulated voltage-dependent conductances, and finish with an analysis of an existing model that has seven voltage-dependent conductances and three distinct [Ca^{2+}] sensors. In all three cases, we examine how the correlations in the steady-state conductance distributions are shaped by the parameters that govern regulation. We find that the intuition developed in the simplest model carries over to more complex cases.

Correlations arise in simple model of homeostatic regulation

The toy (leak) model consists of multiple ohmic conductances with different reversal potentials expressed in a single compartment (schematized in Figure 1a). To provide a biophysical correlate of activity we added first-order Ca^{2+} dynamics with a biologically-realistic decay time-constant (100 ms) and an exponential steady-state dependence on membrane potential, V_m. The Ca^{2+} signal therefore gives a readout of V_m which approximates the way that Ca^{2+} concentration responds to membrane potential fluctuations in biological neurons.

Finally, we added a mechanism that slowly varies each membrane conductance according to activity. To ensure a stable activity level, we postulate a 'target value' for [Ca^{2+}] such that each conductance is up or down-regulated according to the current [Ca^{2+}] level (Methods). For example, the inward conductance g_{in} down-regulates when [Ca^{2+}] is above its target value and up-regulates below it (Figure 1a).

The expression level of each conductance in this model is therefore independently coupled to activity with its own slow dynamics (Figure 1b). It is important that we assume regulation is slow because this corresponds to what is observed experimentally, where homeostatic or compensatory changes in neuronal membrane conductances in many preparations occur over many hours or days (38-40). It also turns out that because regulatory dynamics are much slower than fluctuations in activity, the toy model approximates the way in which complex, voltage dependent conductances shape average activity over similarly slow timescales (41) (see Appendix).

Figure 1c shows the behavior of this model. The model has an outward conductance g_1 (reversal potential, E_{rev} = -90 mV) and two inward conductances, g_2 (E_{rev} = -30 mV) and g_3 (E_{rev} = +50 mV). In all of the traces in Figure 1c, the blue traces show the evolution of a canonical version of the model in which the inward conductances are downregulated when $[Ca^{2+}]$ is above target, and upregulated when $[Ca^{2+}]$ is below target. The outward conductance is regulated in the opposite direction. Each of these conductances has a different time-constant of regulation (Methods).

The light blue traces in Figure 1c show multiple runs initialized with random values for each conductance. The bold traces show the trajectory of the model starting at the average value of this random initial distribution. Note that in this model, the final conductance values are different for each distinct run. We asked how the values of the regulation time-constants influence the evolution of the model by varying each independently. The green traces in Figure 1c show a version of the model in which the time-constants for g_1, g_2 and g_3 are scaled (× 1, × 10, × 40 respectively), resulting in steeper rates of change in this case. In both of these versions of the model, $[Ca^{2+}]$ equilibrates at its target value. Interestingly, when we changed the *sign* of g_2 (thus making its direction of regulation 'anti-homeostatic') the model also converges to target $[Ca^{2+}]$ value (red traces). In fact, homeostatic models with multiple conductances can tolerate such anti-homeostatic regulation in a subset of conductances provided broad constraints on the regulation rates (τ_i) are respected (see below).

How do the regulation rates influence the resulting steady-state distribution of conductances? Figure 1d shows three views of a 3D plot showing the conductances as

they are distributed initially (orange points) and at steady-state. Note that each version of the model (with different sets of regulation rates) converges to a distinct region of conductance space, but these regions sit on a common plane (pink rectangle). This plane is simply the solution set of all conductances that produce target activity in the model. Thus, the regulation rates (as well as the initial values of the conductances) determine the direction in which the model evolves in conductance space, while the point of intersection of each trajectory with the solution plane dictates the steady-state conductance values.

The correlation between each pair of conductances is obtained by projecting the steady-state clouds of points in Figure 1d onto the respective axes. Figure 1e shows distinct pairwise correlations between all three conductances. Changing the regulation rates changes the correlations (panel 2, green) as does making one of the regulation directions antihomeostatic (third panel, red). Thus, correlations emerge from homeostatic rule, and the specifics of the correlations depend on the specifics of the rates governing the insertion and removal of the channels in the membrane.

Mathematically, the pairwise correlations are determined by the geometric relation between the plane and the location of the steady-state points. We calculated the slopes of the correlation between each conductance (black lines in Figure 1e) as follows (full details are in the Appendix). The trajectories of the models' evolution are shown in the 3D plots of Figure 1d. The light blue arrow in the large plot shows the direction of the mean trajectory as it hits the plane, while the pink arrow shows the surface normal of the plane. To calculate the correlation vector at this point we simply resolve the light blue arrow onto the plane as shown (dark blue arrow). The ratios of the components of this correlation vector provide the pairwise correlations in the conductances.

The relationship between the solution plane, the initial conductance values and the direction of the model's trajectory through conductance space (determined by the regulation rates and the form of the regulatory rule) dictates whether or not the model converges to stable target behavior. Intuitively, as long as the net movement of the trajectory is toward the plane the regulation rule will converge. Many combinations of regulation rates achieve this (see Appendix). For example, if expression rates and signs

(i.e. directions) are chosen at random in this toy model, over half (62%) of the resulting models produce stable target activity with conductance values inside reasonable bounds (< 1 mS/nF).

Thus the stability of homeostatic regulation is relatively insensitive to the regulation rates. Moreover, because the rates determine correlations, there is a large amount of freedom to determine the direction and magnitude of correlations between conductances. This is a robust mechanism by which distinct cell types can maintain distinct correlations in their conductances.

Correlations emerge in a homeostatically-regulated spiking model

A simple leak model is intuitive to understand and straightforward to work with mathematically, but the most widely-relevant and interesting examples of homeostatic regulation involve voltage-dependent conductances. The dynamics of regulation in these more complex cases are difficult to study because there is a far more complicated relationship between the distribution of conductances and the resulting activity pattern. It was therefore not immediately clear that the results we obtained for the leak model would carry over to more realistic conductance-based models of spiking neurons. To address this, we constructed a single-compartment, conductance-based model of a spiking neuron with seven voltage-gated conductances, a fixed leak conductance and realistic calcium dynamics. Three of the seven voltage-gated conductances (A-type potassium, g_{KA}, delayed rectifier, g_{Kd}, and hyperpolarization-activated mixed cation conductance g_{H}) in this model are controlled by the same homeostatic regulation rule as in the toy model with a single intracellular [Ca^{2+}] target. The remaining conductances are fixed at values that generate tonically-spiking behavior over a range of randomly-chosen initial values for the three regulated conductances (Methods).

Figure 2a shows the evolution of [Ca^{2+}] in this model for three different sets of regulation rates. As with the toy model, we fixed a default set of rates (blue traces) and from these defined a 'scaled' set ($0.5 \times \tau_{\mathrm{gKA}}$, $2 \times \tau_{\mathrm{gH}}$, green traces) and a 'flipped' set ($-1 \times \tau_{\mathrm{H}}$, red traces). All three sets of rates produce models whose average [Ca^{2+}] converges to the homeostatic target. Figure 2b shows membrane potential activity at

different timepoints in the evolution of each version of the model. The random initial conductance distribution produces spiking neurons with high firing rates (~30 Hz) and, as a result, $[Ca^{2+}]$ is above target. Over time, all three versions of the model converge to a set of conductances that have a lower firing frequency and qualitatively different spike shapes (Figure 2c).

The steady-state conductance distributions for this model are shown in the 3D plots in Figure 2d. In this region of conductance space, the sets of solutions that give target [Ca2+] are seen to sit on a surface that is close to being planar. Again, these solutions give rise to pairwise correlations between the three regulated conductances, as can be seen in the correlation plots at the bottom of Figure 2d. Thus in spite of the complex, non-linear relationship between the dynamics of the voltage-dependent conductances in this model and membrane potential activity, the steady-state conductances distribution behaves in a similar way to the toy model. This will not be true in for all regions of parameter space because it is known that the solution spaces for a particular type of activity can be complex and exhibit abruptly dependences on the maximal conductances. However, locally, these solution spaces can often be well-approximated by a flat space owing to the smooth dependence of quantities such as 'average calcium concentration' on maximal conductances (see Appendix). The toy model is therefore a useful tool for understanding general properties of homeostatic regulation.

Correlation structure in a seven-conductance homeostatic model

The toy model of homeostatic regulation explains, in part, how correlations can arise in the conductance distributions of real neurons, as has been observed recently (29, 42) and makes a strong prediction about the behavior of more complex and realistic regulatory models. Specifically, the simplified model predicts that regulatory control mechanisms that independently tune multiple conductance densities according to a target activity level impose a correlation structure on the steady-state conductance distribution. Furthermore, it predicts that a subset of membrane conductances can be regulated anti-homeostatically and this can nonetheless produce target behavior, but with a different final conductance distribution for a given range of initial conditions. To

investigate this prediction in a more realistic situation with multiple nonlinear conductances and multiple activity sensors, we examined how regulation shapes steady-state conductance distributions in an existing, complex model of a self-regulating rhythmically-bursting cell developed in Liu et al. (13)

The Liu et al. model has seven voltage-dependent conductances plus a leak conductance (see Methods), a Ca^{2+} buffering mechanism and three activity sensors that depend on calcium influx through the two voltage-gated Ca^{2+}conductances. These sensors act as filters that decompose the Ca^{2+} signal into three bands: a fast band corresponding to Ca^{2+} transients caused by spikes, a slow band corresponding to Ca^{2+} waves that generate rhythmic bursting and a steady-state band that measures average Ca^{2+} influx. The regulatory control mechanism imposes a target on each sensor that was empirically chosen (13) to generate bursting models with dynamics similar to crustacean pacemaker neurons. This model thus has a high-dimensional conductance space and multiple constraints imposed by its regulatory mechanism.

We generated a population of 9370 Liu et al. model neurons by initializing each cell with uniform, randomly-distributed maximal conductances and allowing the conductance distribution to reach steady state. An example run is shown in Figure 3a, where it is important to note the short timescale of convergence. This timescale, determined by a short conductance regulation time-constant of 5 seconds, does not mirror the biology, but was necessary to make repeated simulations of this model practical and does not qualitatively change the steady-state solution (13). 8087 models (86%) from this initial population converged to a steady-state with sensor values equal to their targets (Methods). The resulting conductance distribution for these models is shown in Figure 3b, where the values of the maximal conductances have been restricted to physiologically reasonable bounds. The relationship between the maximal conductances in this solution space is clearly more complex than can be described by straightforward linear correlations as in the simpler models of Figures 1 and 2. This is to be expected given the highly non-linear relationship between the effects of each of the model's conductances on the three activity sensors. Nonetheless, a clear pattern is evident in the pairwise plots of maximal conductances (Figure 3b).

The intuition developed in the toy model of Figure 1 tells us that the set of solutions found by a homeostatic mechanism is a subset of all available solutions. To approximate the set of all solutions over a range of conductances in the complex model, we analyzed the membrane potential behavior of 2×10^6 non-regulating model neurons randomly parameterized from a uniform distribution spanning the physiologically realistic range of maximal conductances in the converged, regulated models. Of these random models, we selected 8638 that had membrane potential activity within 10% of the target sensor values. This tolerance corresponds to approximately one standard deviation of the steady-state sensor values in the converged Liu et al. models and was found to be sufficient to determine bursting behavior (Methods). In both regulated and randomly selected models, a wide variety of bursting behaviors is evident as can be seen in the traces in Figure 3d. Furthermore, representatives of the different characteristic behaviors (as delineated by membrane potential waveform, bursting frequency and number of spikes per burst) can be found in both cases.

The correlation structure in membrane conductances of the randomly-selected bursting models is markedly different from the structure observed in models that implement regulatory control to achieve their target activity (Figure 3b-d). This demonstrates that the regulatory control mechanism does indeed impose a characteristic correlation structure on the distribution of conductances as predicted by the analysis of the toy model. In general, the randomly selected solutions exhibit less structure in this distribution, as exemplified in the scatter plots of g_{Na} vs g_{Kd} in Figure 3d. However, certain conductance pairs show a compensatory relationship that is preserved in the Liu models, for example g_{CaS} vs g_{KA} in Figure 3b-c.

Finally, we addressed the question of how the model behaves when conductances are regulated in the 'wrong' direction. The left-hand table in Figure 4a shows the regulation coefficients used in the original model alongside a set of coefficients that was formed changing the signs of the regulatory coefficients of the A-type potassium conductance, g_{KA}. In the original model g_{KA} is up-regulated when either the slow or the steady-state Ca^{2+} sensor is above target and down-regulated when these sensors are below their target level. The sign change in the alternate model causes g_{KA} to be regulated in the opposite way, which is intuitively ‘anti-homeostatic’.

As predicted by the analysis of the simplified model, changing regulation signs in this way causes convergence to a different distribution of final membrane conductances. This can be seen by comparing the correlation maps and histograms in Figure 4b. For example, the distribution of g_{KA} and g_{CaS} is shifted toward lower values, which has a clear effect on the pairwise relation between these two conductances (scatter plots in Figure 4c). On the other hand, the distribution and correlation pattern of g_{KD} and g_{Na} is left relatively unchanged. In spite of this shift in the overall distribution of conductances, target sensor values are achieved and this results in functional bursting behavior as shown in Figure 4c. To make a valid comparison with the behavior of the original model, we used the same random initial conditions. This resulted in fewer models (77%) converging to steady state according to our criteria than in the original model. Perhaps surprisingly, examples that are representative of the diverse range of bursting behaviors in the original model can nevertheless be easily found in the alternate model, as is evident in the example traces in Figure 4c. Thus two different sets of regulation rules find a subset of the available bursting solutions in conductance space, and this distribution is concentrated in a different region for each set of rules. The fact that the alternate model converges to the same functional behavior shows that there is sufficient degeneracy in the dynamical properties of the eight conductances to reach target activity despite the altered regulation rule.

Discussion

Almost twenty years ago, a handful of theoretical studies (10, 12, 27) suggested that stable neuronal function requires some kind of homeostatic regulation of ion channel expression. This triggered a host of experimental studies that are consistent with the idea that nervous systems must balance the mechanisms that allow them to be plastic with others that maintain their stability (5, 39, 40, 43). Subsequently, both theoretical and experimental studies showed that there are multiple solutions consistent with very similar activity patterns (30, 36, 44-47). It is important to recognize that homeostatic tuning rules, such as those studied here, do not invariably produce the same set of channel densities, but instead result in a target activity that is consistent with a range of solutions. It is also important to remember that although homeostatic tuning rules can compensate for many perturbations and for some genetic deletions, they cannot compensate for all deletions of specific currents. Indeed, when there are multiple currents with degenerate, or overlapping functions, compensation occurs easily, but if there is a single current responsible for an important process, homeostatic tuning rules will never achieve perfect compensation upon deletion of this current.

One of the new contributions of the present work is that we have shown that the range of solutions consistent with a particular homeostatic rule has a specific structure that results in correlations in ion channel expression. Thus, the experimental measurements of correlations (28, 29, 32, 34) may provide direct insight into the underlying regulatory rates in biological neurons. Moreover, we now demonstrate that the homeostatic processes themselves can be far sloppier than might have been previously expected. This is comforting, as it reassures us that these kinds of processes can be instantiated in biological systems that have variable and noisy components.

Before relating our modeling results to biology it is important to note the assumptions our work is based on and its potential limitations. The clearest simplifying assumption we have made is the form of the regulatory rule, which simply modulates the rate of expression of different membrane conductances to a Ca^{2+} 'error signal'. Biological neurons employ complex cascades of signal transduction and trafficking mechanisms to control ion channel expression and these mechanisms remain the focus

of intense research (22, 38, 48-50). Our results rely on these underlying pathways approximating a simple feedback rule that depends on intracellular Ca^{2+}concentration. An important task for future work is to relate simplified schemes such as the regulatory rule we employ here to the details of the biological signaling mechanisms as they become available. Nonetheless, existing experimental work that measures the dynamics of homeostatic plasticity and its dependence on mean intracellular Ca^{2+} concentration are consistent with the qualitative behavior of simple models (14, 19, 22).

Homeostasis and degeneracy

Most neurons express upwards of tens of different types of ion channels, and many of these channels overlap in their biophysical properties. For example, several genetically-distinct distinct potassium channels can coexist in a single mammalian neocortical neuron (33) and to some extent these channels perform similar electrophysiological functions. This kind of functional overlap is an example of degeneracy (51, 52) and its existence in membrane conductance properties of ion channels has important implications for homeostatic regulation mechanisms. This observation was first made theoretically by examining the degeneracy present in the map between conductance space and electrophysiological phenotypes, where it is clear that multiple conductance distributions can give rise to electrical properties that are, in biological terms, virtually identical (45, 46, 53). Degeneracy of this kind has been observed experimentally (30) and prompts the question of how neurons regulate multiple conductances to achieve a characteristic electrical behavior. A clue was found in the observation that neurons of a defined type show strong correlations between both mRNA expression and functional expression of different ion channels (28, 29, 42). This led to the idea that correlations provide an important determinant of cell identity by ensuring fixed ratios in the expression of different ion channel types (54). However, it is not known how such correlations are achieved or maintained. Our findings add to this picture by showing that feedback regulation of conductances toward activity set-points constrains the steady-state distribution and that this can produce distinct correlation patterns.

Not only could this effect contribute to observed correlations in experimental measurements of membrane conductances (28, 29, 31-34), but it may also explain why

previous studies that found successful models based on phenomenological properties of neuronal activity failed to replicate biological correlation structures (36, 47, 54). These previous studies randomly sampled the set of membrane conductances in complex, rhythmically bursting neuron models and selected combinations of conductances that reproduced biologically realistic behavior. However, the correlation pattern found by randomly sampling in this way did not resemble correlation patterns in found in experiments – a result that parallels the situation in Figure 3, where randomly-selected models and homeostatically-regulated models exhibit very different conductance distributions. To replicate experimentally-observed correlations in models it may therefore be necessary to obtain a quantitative description of how conductances are regulated with respect to activity as well as the ways that different conductances shape activity. Nonetheless, activity-dependent regulation cannot be thought of as a catch-all for explaining ion channel expression. In biological neurons we expect many constraints to exist besides broad activity targets and these will further shape the solution space. For example, the coordinated expression of ion channels may be coupled to activity-independent processes, such as epigenetic modification of ion channel genes during cell differentiation. Relative expression may also be 'hard-wired' in a way that only makes sense from an evolutionary perspective, including conserved transcriptional control of multiple ion channel genes by a shared transcription factor or regulatory element. Our results are compatible with these kinds of constraints and the extent to which ion channel expression is determined by activity-independent regulation remains an open question.

How conductance correlations are related to expression rates

In all of the models we saw that the shape of the steady-state distribution of conductances depends on the rate at which each conductance is regulated with respect to other conductances. One way to think of this is to imagine a neuron that homeostatically regulates two-pore domain (leak) potassium channels more quickly than persistent sodium channels. In situations where activity is too low, the potassium channels will be rapidly removed from the membrane and the sodium channels will slowly start to accumulate. By the time the activity target is reached, the potassium channels will have undergone a larger change in their expression than the sodium channels. Throughout a population of these hypothetical cells with varying activity histories, one would observe a large range in potassium channel density and a smaller range in sodium channel density, with the two channel types showing correlated expression according to the combinations that achieve the homeostatic target.

In biological neurons it is therefore plausible that differing rates of expression between ion channel subtypes provide a mechanism for determining cell-type signatures in correlated ion channel expression. Viewed in this way, the regulatory mechanisms are a more fundamental determinant of cellular identity than the expression levels of ion channels and mRNAs at a single point in time. This is consistent with the principle that specific transcription factors are often used as cell-type markers, and with the observation that reliable cell-type classification requires the expression of many ion channel genes to be measured combinatorially (33, 55).

Robust regulation from degenerate ion channel function

An important consequence of degeneracy in membrane conductances is that the regulation of all individual conductances in a given neuron need not occur in the 'correct' direction in the homeostatic sense, provided a sufficient subset of remaining conductances is appropriately regulated. Recent work (56) that quantified expression of the transcriptome of murine cortical neurons revealed both up- and down-regulation of inward as well as outward conductances in response to sustained membrane potential depolarization. However, the same manipulation in similar preparations has also been shown to result in a net downregulation of intrinsic excitability (14, 50). Our work here

helps resolve these empirical observations and cautions against focusing on individual genes and proteins when trying to understand compensatory responses.

In general, this indicates that homeostatic mechanisms in neurons leave more 'room for maneuver' in the way individual conductances are regulated than previously appreciated. Indeed, recent experiments indicate that in addition to homeostatic regulation of maximal conductance, the half-activation of voltage-gated conductances can be subject to regulation and that this permits tuning of rebound spiking in dopaminergic cells of the substantia nigra (57).

The advent of high-throughput, multiplexed monitoring of gene expression, protein expression and neuronal activity offers the potential to quantify the level of degeneracy in nervous systems. In principle this will allow us to explore questions that, at present, can only be fully addressed in a theoretical setting, such as how the full complement of ion channels in a population of neurons might be regulated during development and in response to perturbations. Our study highlights the role of degeneracy in homeostatic systems, illustrating the extent to which degeneracy explains variability and enables systems to cope with aberrant regulation of a subset of components. A full understanding of homeostasis in degenerate systems is a therefore a prerequisite to understanding phenotypic variability in nervous systems, and why – in the case of many diseases – the nervous system may not be able to compensate for loss of function.

Methods

All models were single-compartment conductance-based neurons which followed the standard Hodgkin-Huxley formalism. The membrane potential, V, of a cell containing N conductances and total membrane capacitance, C, thus evolves according to:

$$C\frac{dV}{dt} = \sum_{i=1}^{N} \bar{g}_i m_i^{p_i} h_i^{q_i}(V - E_i) \qquad (1)$$

$\bar{g}_i$ is maximal conductance (bar omitted in for leak conductances), p_i and q_i are integers representing the number of independent 'gates' in each conductance, and E_i is the reversal potential. The variables m and h respectively represent the activation and inactivation of each current; h is omitted in non-inactivating currents, while both m and h are omitted in leak currents. All models have unit capacitance (1 nF); maximal conductance values in the manuscript are therefore equivalent to conductances densities in units of μS/nF.

In Figure 1, we analyze conductance regulation in a model cell containing three leak conductances (g_1, g_2, g_3) with reversal potentials of E_1 = 90, E_2 = -30, and E_3 = +50. The calcium dynamics of this model were implemented as follows:

$$\tau_c \frac{dc}{dt} = c_\infty(V_m) - c \text{ , where } \quad c_\infty(V_m) = A\exp(bV_m) \qquad (2)$$

Calcium concentration, c, is thus modeled with linear first-order dynamics with time-constant τ_c = 100 ms. The steady-state calcium concentration was based on a least-squares fit of the steady-state calcium in the Liu et al. model(13) (see below) over the membrane potential range -80 to -20 mV, giving A = 109.2 μM, b = 0.08 mV^{-1}.

Unless specified the maximal conductances in all models $\bar{g}_i$ are dynamically adjusted by a calcium-dependent regulation rule. Specifically, the conductances change over time according to the equation(13):

$$\tau_i \frac{d\bar{g}_i}{dt} = \Gamma\bar{g}_i \ , \qquad (3)$$

In this equation, Γ is the "error function" which is dependent on the calcium current. We observe the convention by which $\Gamma < 0$ when the calcium current is below its target activity profile, and $\Gamma > 0$ when the calcium current is above target. The time constants, τ_i, in equation 3

scale the rate of conductance regulation and determine the direction of regulation (for example, if $\tau_i > 0$, then $\bar{g}_i$ increases when $\Gamma > 0$ and decreases when $\Gamma < 0$).

In Figure 1, we set $\Gamma = \Gamma(c) = c - c_T$, where $c_T = 1\,\mu$M, is the target intracellular calcium concentration. The values for τ_i (in seconds) used in the original model in Figure 1 are: $\tau_1 = +4 \times 10^3$, $\tau_2 = -6 \times 10^3$, and $\tau_3 = -1 \times 10^3$. The traces in Figure 1 were obtained by numerically integrating (3) for 10^5 s (~27.8 hours simulated time). Initial values for the three conductances were randomly chosen from Gaussian distributions (truncated below zero) with means ± standard deviations (in μS/nF) as follows: 105 ± 2.5 (g_1), 20 ± 2.5 (g_2) and 10 ± 2.5 (g_3). The details of the analysis of this model are in the Appendix.

In Figures 2-4, we examine a model neuron with a passive leak current (g_L) and seven voltage-dependent currents: fast sodium (g_{Na}), delayed rectifier (g_{Kd}), fast transient calcium (g_{CaT}), slow calcium (g_{CaS}), calcium-dependent potassium (g_{KCa}), fast transient potassium (g_A), and a hyperpolarization-activated inward cation current (g_H). The leak reversal potential was −50 mV, potassium, −80 mV and sodium +50 mV. Calcium reversal potential was dynamically calculated from the Nernst equation assuming an extracellular concentration of 3 mM. The equations describing the voltage-dependence and the kinetics of these currents and Ca^{2+} dynamics are given in the Appendix of Liu et al.(13)

The spiking model of Figure 2 used the same regulation rule as the toy model but with the time-constants of regulation for g_A, g_{Kd} and g_H set (in ms) to -7.5×10^3, -5×10^3 and $+5 \times 10^2$ respectively. The remaining maximal conductances were fixed at the following values (in μS/nF): g_{Na} = 100, g_{CaS} = 0.5, g_{CaT} = 0.5, g_{KCa} = 10, g_L = 0.01. Initial values for the three regulated conductances (in μS/nF) were uniformly randomly chosen in the ranges 40 ± 5 (g_{Kd}), 10 ± 1.25 (g_A) and 0.5 ± 0.0625 (g_H).

In Figures 3 and 4, we examine the conductance regulation model as originally described in Liu et al. In this model, the error function is not a direct function of intracellular calcium concentration, but rather depends on three calcium sensors which filter the calcium signal into distinct frequency bands. The activation of each sensor is represented by three variables F, S, and D (the letters represent the time scale of each sensor; “fast”, “slow”, and “DC”), which are calculated at each time point according to the equations:

$$F = G_F M_F^2 H_F \ , \quad S = G_S M_S^2 H_S \ , \quad D = G_D M_D^2 \ . \qquad (4)$$

The form of the above equations is similar to a typical Hodgkin-Huxley channel model: the H and M variables are analogous to the activation and inactivation gating variables, and the G parameters are analogous to the maximal conductance. Following the parameters reported in Liu et al., we set $G_F = 10$, $G_S = 3$, and $G_D = 1$. Each M and H variable were numerically integrated according to:

$$\tau_{M_X} \frac{dM_X}{dt} = \frac{1}{1 + \exp[Z_{M_X} + I_{Ca}]} - M_X \quad (5)$$

$$\tau_{H_X} \frac{dH_X}{dt} = \frac{1}{1 + \exp[-Z_{H_X} - I_{Ca}]} - H_X \ . \quad (6)$$

Here, X substitutes for each sensor in the model ($F, S,$ or D), the Z_M and Z_H parameters respectively control the half-activation and half-inactivation of point of the steady-state curves for M and H, and the τ_M and τ_H parameters scale the rate at which the M and H variables change over time. The values for the Z_M, Z_H, τ_M, and τ_H parameters are given in Table 2 in Liu et al. The conductances are regulated according to:

$$\tau_g \frac{d\bar{g}_i}{dt} = \Gamma_i \bar{g}_i = [A_i(\bar{F} - F) + B_i(\bar{S} - S) + C_i(\bar{D} - D)]\bar{g}_i \ , \quad (7)$$

Where A_i, B_i, and C_i are constant coefficients equal to -1, 0, or 1, and are distinct for each regulated maximal conductance (see Figure 4A for their values in the original and "alternate" model). The parameters $\bar{F}$, $\bar{S}$, and $\bar{D}$ represent the target activation level for each sensor; as in Liu et al., they were all set equal to 0.1 as this was empirically found to produce bursting cells(13) . Each conductance is regulated with time constant $\tau_g = 5$ seconds that was not found to interact with the faster dynamics of the system (membrane potential and Ca^{2+})(13). Thus, the coefficients A_i, B_i, and C_i collectively the direction of conductance regulation, while τ_g scales the rate of regulation.

The initial conductances for Figures 3 and 4 were randomly drawn from a uniform distribution (the maximal conductances for g_{Na}, g_{Kd}, g_A, and g_{KCa} were selected between 2.5 and 47.5 μS/nF, while the maximal conductances for g_{CaT}, g_{CaS}, and g_H were selected between 0.05 and 0.95 μS/nF). The chosen initial ranges for Figures 3 and 4 were empirically found to produce a high proportion of models with final conductances that fit within a range that is both physiologically realistic and tractable to search randomly (Figure 4, 'random models').

All homeostatically regulated models in Figures 3 and 4 were simulated for an hour of simulated time. Though many simulations converged to a stable solution on a faster time scale (under 10 minutes simulated time), certain initial conditions required much longer to reach a stable solution set. As observed by Liu et al., a small subset of initial conditions did not converge during the simulation. To exclude non-converging models, we discarded simulations in which any of the maximal conductances had coefficients of variation above 0.015 over the last 30 simulated seconds; 14% of all models with the original Liu et al. regulation coefficients (Left Panels in Figure 3B and 4B) were excluded according to this criterion, while in the alternate model (Right Panel in Figure 4B) this proportion was 23%. For the purpose of performing a random search in conductance space, the scatter plots and histograms in Figure 3 are restricted to ranges that we considered to be physiologically realistic, in μS/nF these are zero through 146 (g_{Na}), 2.9 (g_{CaT}), 5.4 (g_{CaS}), 134 (g_{KA}), 134 (g_{KCa}), 69 (g_{Kd}) and 0.8 (g_{H}). Those in Figure 4 are extended three-fold to show the full structure of the distributions.

Appendix: mathematical analysis of conductance regulation

Here we analyze the regulatory system in the case of a single calcium sensor, i.e. when regulation is just a function of instantaneous calcium concentration. For the toy model we can derive explicit expressions for the conductance correlations and conditions for convergence/stability of the regulatory system. The more complex voltage-dependent case is similar locally. The details of how average calcium concentration depends on each of the conductances will determine how well local behavior approximates global behavior in specific cases.

The equations for the toy model are:

$$C_m \frac{dV}{dt} = \sum_i g_i(E_i - V)$$

$$\tau_{\mathrm{Ca}} \frac{d[\mathrm{Ca}^{2+}]}{dt} = (c(V) - [\mathrm{Ca}^{2+}])$$

$$\tau_i \frac{dg_i}{dt} = g_i([\mathrm{Ca}^{2+}] - c_T)$$

Where C_m is (unit = 1 nF) membrane capacitance, V is membrane potential, g_i is conductance, E_i is the reversal potential corresponding to each conductance, τ_{Ca} is calcium decay timeconstant, $c(V)$ is the membrane potential-dependent steady-state calcium concentration (Methods), τ_i is the conductance regulation timeconstant and c_T is the calcium concentration target.

For slow regulation we can assume $\tau_i {g_i}^{-1} \gg \tau_{\mathrm{Ca}}, \tau_m$ (where τ_m is the membrane time-constant) and we replace V and $[\mathrm{Ca}^{2+}]$ with their steady-state values. This results in an autonomous system of equations in the conductances alone:

$$\dot{g}_i = \omega_i g_i u(\boldsymbol{g}) \qquad (1)$$

Where the dot indicates time derivative, $\boldsymbol{g} = (\dots, g_i, \dots)$ and we have written $u(\boldsymbol{g}) = c(V(g)) - c_T$ and $\omega_i = \tau_i^{-1}$ for convenience. Unfortunately, this system is nonlinear and cannot be solved explicitly (as a function of time) by standard methods. We can, however, describe the locus of the solution trajectory in the toy model. We can also

derive conditions for stability and determine the pairwise correlations at steady-state in more general cases.

The solution space

The solution space for the toy model is obtained by setting equation (1) to zero, which results in a (hyper) plane equation in $\boldsymbol{g}$:

$$0 = \sum_i g_i(E_i - V^{ss}) = \boldsymbol{g} \cdot \boldsymbol{n} \qquad (2)$$

Where $\boldsymbol{n} = (E_i - V^{ss})$ and $V^{ss} = c^{-1}(c_T)$.

A more general case with voltage-dependent conductances has a similar expression for the solution set, namely:

$$0 = \sum_i g_i(\langle V \rangle)(E_i - \langle V \rangle).$$

Where $\langle V \rangle$ denotes the mean membrane potential at (quasi) steady-state. This equation no longer defines a hyperplane due to the dependence of g_i on $\langle V \rangle$. It is, however, locally approximated by a plane of the form (2) by setting the g_i to their value at a particular equilibrium solution. The general solution space is thus an (n-1) manifold (possibly containing singularities where the steady-state is unstable or when membrane potential activity abruptly changes with variation in a conductance). This relates the toy model to more complex models involving voltage-dependent conductances.

Determining correlations and convergence

Equation (1) defines the direction of the flow of the system at any point in conductance space. The pairwise correlations can be computed in general by resolving the flow vector onto the solution space near an equilibrium point. We write the system as:

$$\dot{g}_i \stackrel{\text{def}}{=} F_i.$$

Linearizing about a point in conductance space ($\boldsymbol{g}^0$) and rewriting $\boldsymbol{g} \leftarrow\!\shortmid \boldsymbol{g} - \boldsymbol{g}^0$ gives

$$\dot{\boldsymbol{g}} = \boldsymbol{A}\boldsymbol{g}$$

where $\boldsymbol{A} = \frac{\partial F_i}{\partial g_j}$. The direction of flow is therefore given by $\boldsymbol{Ag}$. The correlation vector, $\boldsymbol{g}^{\text{corr}}$, is then computed at $\boldsymbol{g}^0$ as follows:

$$\boldsymbol{g}^{\text{corr}} = \boldsymbol{A}\boldsymbol{g}^0 - \langle \boldsymbol{A}\boldsymbol{g}^0, \hat{\boldsymbol{n}} \rangle \hat{\boldsymbol{n}} \qquad (3)$$

where $\hat{\boldsymbol{n}}$ is the unit normal vector to the solution plane, $\hat{\boldsymbol{n}} = \boldsymbol{n}/\|\boldsymbol{n}\|$ defined in (2). Pairwise correlations are then obtained from the ratios of the components of $\boldsymbol{g}^{\text{corr}}$. This shows explicitly how the correlations depend on the expression rates of each conductance for arbitrary regulation rules.

For example, for the toy model, $\boldsymbol{A}$ becomes:

$$\boldsymbol{A} = \left\{ \omega_i g_i \frac{\partial u}{\partial g_j} - \omega_i g_i u \delta_{i,j} \right\}_{i,j} \qquad (4)$$

where $\delta_{i,j}$ is the Kronecker delta symbol. Substituting this into (3) and using the equation for $\boldsymbol{n}$ defined in (2) gives an explicit expression for the correlations in terms of the parameters of the model. This calculation was used to produce the correlation lines in Figure 1(e).

Alternatively, single-sensor models permit the loci of the trajectories to be determined by taking the quotients the derivatives of each conductance defined in (1) when $[\text{Ca}^{2+}] \neq c_T$:

$$\frac{\dot{g}_i}{\dot{g}_j} = \frac{\omega_i g_i}{\omega_j g_j} \quad \text{so,} \quad \int \frac{\dot{g}_i}{g_i} dt = \frac{\omega_i}{\omega_j} \int \frac{\dot{g}_j}{g_j} dt$$

This gives $g_i = r g_j^{\tau_j/\tau_i}$ for each i, j with r determined by the initial values of each conductance, $r = g_i(0) g_j(0)^{-\tau_j/\tau_i}$. Solutions (where they exist) are therefore given by solutions to the following system of equations, which define the intersection points of the trajectory loci with the solution plane:

$$\left.\begin{aligned} 0 &= \sum_i g_i (E_i - V^{ss}) \\ g_i &= g_i(0) g_j(0)^{-\tau_j/\tau_i} g_j^{\tau_j/\tau_i} \end{aligned}\right\} \forall i, j$$

The existence of strictly positive solutions to this system on the branch of the locus in which the trajectory moves provides a criterion for the convergence of the homeostatic rule.

Numerically, the system described in Figure 1 converges in 62% of cases (6151 out of 10,000 simulations) where the regulation rates are randomly chosen on the ball defined by $\|\boldsymbol{\tau}\| = 10^4$ s, $\boldsymbol{\tau} = (\dots, \tau_i, \dots)$.

The Linearization also allows us to provide explicit necessary conditions for stability at steady-state. Imposing steady-state conditions in (4), $\boldsymbol{A}$ becomes:

$$\boldsymbol{A} = \left\{ \omega_i g_i \frac{\partial u}{\partial g_j} \right\}_{i,j} = \boldsymbol{a} \otimes \boldsymbol{b}$$

where $\otimes$ denotes outer product, $\boldsymbol{a} = (\dots, \omega_i g_i, \dots)$ and $\boldsymbol{b} = (\dots, \frac{\partial u}{\partial g_i}, \dots)$.

The characteristic equation of this linearization is therefore:

$$\left| \boldsymbol{a} \otimes \boldsymbol{b} - \lambda \delta_{i,j} \right| = (\lambda - \boldsymbol{a} \cdot \boldsymbol{b}) \lambda^{n-1}$$

This has $n - 1$ degenerate solutions $\lambda = 0$ and a single solution, $\lambda_1 = \boldsymbol{a} \cdot \boldsymbol{b} = \sum_{\boldsymbol{i}} \omega_i g_i \frac{\partial u}{\partial g_i}$.

The zero eigenvalues prevent us from rigorously deriving sufficient conditions for stability using the linearization. We can, however, provide necessary conditions by considering the unstable case, $\lambda_1 > 0$. Now,

$$\frac{\partial u}{\partial g_i} = \left. \frac{dc}{dV} \right|_{ss} . \left. \frac{\partial V}{\partial g_i} \right|_{ss} = \left. \frac{dc}{dV} \right|_{ss} . \frac{(V_{ss} - E_i)}{G}$$

where $G = \sum_{\boldsymbol{i}} g_i$. Therefore the condition $\lambda_1 > 0$ implies

$$\boldsymbol{a} \cdot \boldsymbol{b} = \sum_{\boldsymbol{i}} \omega_i g_i (V^{ss} - E_i) > 0.$$

So necessary conditions for stability are:

$$\sum_{\boldsymbol{i}} \frac{g_i}{\tau_i} (E_i - V^{ss}) > 0.$$

This is intuitively clear since $E_i - V^{ss}$ are just the components of the normal to the solution space; i.e. for the system to be stable, trajectories must not move away from the solution plane when perturbed.

Acknowledgements

We thank members of the Marder lab especially Tilman Kispersky and Ted Brookings for helpful comments. We also thank Mark Adler and Thierry Emonet for useful mathematical comments. Supported by NIH grant MH 46742 and the Swartz Foundation.

References

1. Bean, B.P. The action potential in mammalian central neurons. *Nat Rev Neurosci* **8**, 451-465 (2007).
2. Coetzee, W.A.*, et al.* Molecular diversity of K+ channels. *Ann N Y Acad Sci* **868**, 233-285 (1999).
3. Herrera-Valdez, M.A.*, et al.* Relating ion channel expression, bifurcation structure, and diverse firing patterns in a model of an identified motor neuron. *J Comput Neurosci* (2012).
4. Hille, B. *Ion channels of excitable membranes* (Sinauer, 2001).
5. Marder, E. & Goaillard, J.M. Variability, compensation and homeostasis in neuron and network function. *Nat Rev Neurosci* **7**, 563-574 (2006).
6. Marder, E. Variability, compensation, and modulation in neurons and circuits. *Proc Natl Acad Sci U S A* **108**, 15542-15548 (2011).
7. Marder, E. & Prinz, A.A. Modeling stability in neuron and network function: the role of activity in homeostasis. *Bioessays* **24**, 1145-1154 (2002).
8. O'Leary, T. & Wyllie, D.J.A. Neuronal homeostasis: time for a change? *J Physiol* **589**, 4811-4826 (2011).
9. Turrigiano, G. Homeostatic signaling: the positive side of negative feedback. *Current Opinion in Neurobiology* **17**, 318-324 (2007).
10. Abbott, L. & LeMasson, G. Analysis of neuron models with dynamically regulated conductances. *Neural Computation* **5**, 823-842 (1993).
11. Desai, N.S., Rutherford, L.C. & Turrigiano, G.G. Plasticity in the intrinsic excitability of cortical pyramidal neurons. *Nature Neuroscience* **2**, 515-520 (1999).
12. LeMasson, G., Marder, E. & Abbott, L.F. Activity-dependent regulation of conductances in model neurons. *Science* **259**, 1915-1917 (1993).
13. Liu, Z., Golowasch, J., Marder, E. & Abbott, L.F. A model neuron with activity-dependent conductances regulated by multiple calcium sensors. *J Neurosci* **18**, 2309-2320 (1998).
14. O'Leary, T., van Rossum, M.C.W. & Wyllie, D.J.A. Homeostasis of intrinsic excitability in hippocampal neurones: dynamics and mechanism of the response to chronic depolarization. *J Physiol* **588**, 157-170 (2010).
15. Ramakers, G.J., Corner, M.A. & Habets, A.M. Development in the absence of spontaneous bioelectric activity results in increased stereotyped burst firing in cultures of dissociated cerebral cortex. *Exp Brain Res* **79**, 157-166 (1990).
16. Seeburg, D.P. & Sheng, M. Activity-induced Polo-like kinase 2 is required for homeostatic plasticity of hippocampal neurons during epileptiform activity. *J Neurosci* **28**, 6583-6591 (2008).
17. Stemmler, M. & Koch, C. How voltage-dependent conductances can adapt to maximize the information encoded by neuronal firing rate. *Nature Neuroscience* **2**, 521-527 (1999).
18. Triesch, J. A gradient rule for the plasticity of a neuron's intrinsic excitability. *Artificial Neural Networks: Biological Inspirations - ICANN 2005, Proceedings Pt 1* **3696**, 65-70 (2005).
19. Turrigiano, G., Abbott, L.F. & Marder, E. Activity-dependent changes in the intrinsic properties of cultured neurons. *Science* **264**, 974-977 (1994).
20. van Welie, I., van Hooft, J.A. & Wadman, W.J. Homeostatic scaling of neuronal excitability by synaptic modulation of somatic hyperpolarization-activated Ih channels. *Proc Natl Acad Sci U S A* **101**, 5123-5128 (2004).
21. Wierenga, C.J., Walsh, M.F. & Turrigiano, G.G. Temporal Regulation of the Expression Locus of Homeostatic Plasticity. *J Neurophysiol* (2006).
22. Wheeler, D.G.*, et al.* Ca(V)1 and Ca(V)2 channels engage distinct modes of Ca(2+) signaling to control CREB-dependent gene expression. *Cell* **149**, 1112-1124 (2012).

23. Desarmenien, M.G. & Spitzer, N.C. Role of calcium and protein kinase C in development of the delayed rectifier potassium current in Xenopus spinal neurons. *Neuron* **7**, 797-805 (1991).
24. Pratt, K.G. & Aizenman, C.D. Homeostatic regulation of intrinsic excitability and synaptic transmission in a developing visual circuit. *J Neurosci* **27**, 8268-8277 (2007).
25. Tong, H.*, et al.* Regulation of Kv channel expression and neuronal excitability in rat medial nucleus of the trapezoid body maintained in organotypic culture. *J Physiol* **588**, 1451-1468 (2010).
26. Mee, C.J., Pym, E.C., Moffat, K.G. & Baines, R.A. Regulation of neuronal excitability through pumilio-dependent control of a sodium channel gene. *J Neurosci* **24**, 8695-8703 (2004).
27. Siegel, M., Marder, E. & Abbott, L.F. Activity-dependent current distributions in model neurons. *Proc Natl Acad Sci U S A* **91**, 11308-11312 (1994).
28. Schulz, D.J., Goaillard, J.M. & Marder, E. Variable channel expression in identified single and electrically coupled neurons in different animals. *Nature Neuroscience* **9**, 356-362 (2006).
29. Schulz, D.J., Goaillard, J.M. & Marder, E.E. Quantitative expression profiling of identified neurons reveals cell-specific constraints on highly variable levels of gene expression. *Proc Natl Acad Sci U S A* **104**, 13187-13191 (2007).
30. Swensen, A.M. & Bean, B.P. Robustness of burst firing in dissociated purkinje neurons with acute or long-term reductions in sodium conductance. *J Neurosci* **25**, 3509-3520 (2005).
31. Temporal, S.*, et al.* Neuromodulation independently determines correlated channel expression and conductance levels in motor neurons of the stomatogastric ganglion. *J Neurophysiol* **107**, 718-727 (2012).
32. Tobin, A.E., Cruz-Bermudez, N.D., Marder, E. & Schulz, D.J. Correlations in ion channel mRNA in rhythmically active neurons. *PLoS One* **4**, e6742 (2009).
33. Toledo-Rodriguez, M.*, et al.* Correlation maps allow neuronal electrical properties to be predicted from single-cell gene expression profiles in rat neocortex. *Cerebral Cortex* **14**, 1310-1327 (2004).
34. Liss, B.*, et al.* Tuning pacemaker frequency of individual dopaminergic neurons by Kv4.3L and KChip3.1 transcription. *EMBO J* **20**, 5715-5724 (2001).
35. Veys, K., Labro, A.J., De Schutter, E. & Snyders, D.J. Quantitative single-cell ion-channel gene expression profiling through an improved qRT-PCR technique combined with whole cell patch clamp. *J Neurosci Methods* **209**, 227-234 (2012).
36. Taylor, A.L., Goaillard, J.M. & Marder, E. How Multiple Conductances Determine Electrophysiological Properties in a Multicompartment Model. *J Neurosci* **29**, 5573-5586 (2009).
37. Soto-Trevino, C., Thoroughman, K.A., Marder, E. & Abbott, L.F. Activity-dependent modification of inhibitory synapses in models of rhythmic neural networks. *Nature Neuroscience* **4**, 297-303 (2001).
38. Davis, G.W. Homeostatic control of neural activity: from phenomenology to molecular design. *Annu Rev Neurosci* **29**, 307-323 (2006).
39. Desai, N.S. Homeostatic plasticity in the CNS: synaptic and intrinsic forms. *J Physiol Paris* **97**, 391-402 (2003).
40. Turrigiano, G.G. Homeostatic plasticity in neuronal networks: the more things change, the more they stay the same. *Trends in Neurosciences* **22**, 221-227 (1999).
41. Alon, U. *An introduction to systems biology : design principles of biological circuits* (Chapman & Hall/CRC, Boca Raton, Fla. ; London, 2007).
42. Tobin, A.E., Cruz-Bermudez, N.D., Marder, E. & Schulz, D.J. Correlations in Ion Channel mRNA in Rhythmically Active Neurons. *PLoS One* **4** (2009).
43. Turrigiano, G.G. & Nelson, S.B. Homeostatic plasticity in the developing nervous system. *Nat Rev Neurosci* **5**, 97-107 (2004).
44. Aizenman, C.D., Huang, E.J. & Linden, D.J. Morphological correlates of intrinsic electrical excitability in neurons of the deep cerebellar nuclei. *J Neurophysiol* **89**, 1738-1747 (2003).

45. Prinz, A.A., Billimoria, C.P. & Marder, E. Alternative to hand-tuning conductance-based models: Construction and analysis of databases of model neurons. *J Neurophysiol* **90**, 3998-4015 (2003).
46. Prinz, A.A., Bucher, D. & Marder, E. Similar network activity from disparate circuit parameters. *Nature Neuroscience* **7**, 1345-1352 (2004).
47. Taylor, A.L., Hickey, T.J., Prinz, A.A. & Marder, E. Structure and visualization of high-dimensional conductance spaces. *J Neurophysiol* **96**, 891-905 (2006).
48. Spitzer, N.C. A developmental handshake: neuronal control of ionic currents and their control of neuronal differentiation. *J Neurobiol* **22**, 659-673 (1991).
49. Weston, A.J. & Baines, R.A. Translational regulation of neuronal electrical properties. *Invert Neurosci* **7**, 75-86 (2007).
50. Grubb, M.S. & Burrone, J. Activity-dependent relocation of the axon initial segment fine-tunes neuronal excitability. *Nature* **465**, 1070-U1131 (2010).
51. Edelman, G.M. & Gally, J.A. Degeneracy and complexity in biological systems. *Proc Natl Acad Sci U S A* **98**, 13763-13768 (2001).
52. Tononi, G., Sporns, O. & Edelman, G.M. Measures of degeneracy and redundancy in biological networks. *Proc Natl Acad Sci U S A* **96**, 3257-3262 (1999).
53. Goldman, M.S., Golowasch, J., Marder, E. & Abbott, L.F. Global structure, robustness, and modulation of neuronal models. *J Neurosci* **21**, 5229-5238 (2001).
54. Hudson, A.E. & Prinz, A.A. Conductance Ratios and Cellular Identity. *Plos Computational Biology* **6** (2010).
55. Khazen, G., Hill, S.L., Schurmann, F. & Markram, H. Combinatorial expression rules of ion channel genes in juvenile rat (Rattus norvegicus) neocortical neurons. *PLoS One* **7**, e34786 (2012).
56. Kim, T.K.*, et al.* Widespread transcription at neuronal activity-regulated enhancers. *Nature* **465**, 182-187 (2010).
57. Amendola, J., Woodhouse, A., Martin-Eauclaire, M.F. & Goaillard, J.M. Ca(2)(+)/cAMP-sensitive covariation of I(A) and I(H) voltage dependences tunes rebound firing in dopaminergic neurons. *J Neurosci* **32**, 2166-2181 (2012).

Figure Legends

Figure 1. A toy model of activity-dependent conductance regulation.

(a) Schematic of a neuron with regulated inward (g_{in}) and outward (g_{out}) conductances. Inward conductances promote Ca^{2+} influx through voltage-gate calcium channels (red) by depolarizing the membrane potential, while outward conductances inhibit Ca^{2+} influx. In turn, Ca^{2+} influx upregulates the outward current, and downregulates the inward current possibly via modulation of transcription rates or ion channel trafficking dynamics (grey circle). **(b)** A simplified model neuron with three Ohmic conductances g_1, g_2, and g_3, each with a different reversal potential (-90 mV, -30 mV and +50 mV respectively). Calcium dynamics are first-order with exponential steady-state dependence on membrane potential, $c(V_m)$ (Methods) and each conductance is regulated with a specific regulation time constant, τ_i, according to the difference between $[Ca^{2+}]$ and a target value, c_t **(c)** Behavior of three versions of the model with different sets of regulation rates. The traces show the evolution of the three conductances and internal $[Ca^{2+}]$ in 30 simulations of each version of the model. Blue traces = original rates (τ_1, τ_2, τ_3), green traces = scaled rates ($\tau_2 \longmapsto 10 \times \tau_2, \tau_3 \longmapsto 40 \times \tau_3$), red traces = g_2 rate flipped ($\tau_2 \longmapsto -\tau_2$). **(d)** Steady-state conductance distributions. 3D plots showing all three conductances for 300 runs using each of the three sets of regulation rates (orange points = random initial values, blue = original rates, green = scaled rates, red = rate flipped). Each 3d plot is a different view of the same data and the colored curves are the sample trajectories plotted in (c). The large plot to the right shows the calculated solution space of conductance values that give target $[Ca^{2+}]$ (pink plane). The arrows represent the surface normal of the solution plane (pink), the velocity vector for the trajectory of the mean model trace with the original rate set (light blue) and the vector obtained by projecting this velocity vector onto the solution plane (dark blue). **(e)** Scatterplot matrices showing pairwise scatterplots (off-diagonals) between the three maximal conductances in each version of the model. Histograms (diagonals) show the distribution of each maximal conductance by itself. Black lines in each scatterplot are the correlations predicted by resolving the model trajectory onto the solution set

(Methods) as illustrated in the right-hand plot of (d). The schematic to the right of the plots show how the axes in the plots are organized.

Figure 2. Behavior of the simple model is recapitulated in a model with active conductances.

Behavior of a spiking model neuron with a three regulated voltage-dependent conductances controlled by the simple regulatory rule in Figure 1b. Three versions of the model are shown with the regulation rates at their original values ($\tau_{gA}, \tau_{gKd}, \tau_{gH}$, blue plots, see Methods), scaled ($\tau_{gA} \longmapsto 0.5 \times \tau_{gA}, \tau_{gH} \longmapsto 2 \times \tau_{gH}$, green), and with the regulation rate for g_{H} flipped ($\tau_{gH} \longmapsto -\tau_{gH}$, red). **(a)** Example traces of [Ca^{2+}] in each of the three versions of the model. **(b)** Example membrane potential traces at different time-points (1, 2, 3) for each version of the model (timescale = 400 ms) **(c)** Example traces showing the evolution of the three regulated conductances in 30 simulations of each version of the model. **(d)** (Upper panels) 3D scatterplot showing the steady-state conductance distributions for 300 model simulations with each set of rates. The two plots show two rotated views of the same data. (Lower panels) Correlation plots of steady-state conductances for each version of the model.

Figure 3. Structure of the steady-state conductance distribution in a complex homeostatic model neuron. Behavior of a complex bursting model neuron with a seven regulated voltage-dependent conductances and a regulation rule that uses three [Ca^{2+}] sensors **(a)** Evolution of the maximal conductances over time for a single regulated neuron. Example voltage traces at three time points along the evolution trajectory are shown at right, showing that the model converges to the target bursting behavior (horizontal line = 0 mV). **(b)** Pairwise scattergrams (off-diagonals) and histograms (diagonals) of the final values for the 7 regulated maximal conductances after one hour of simulated time. Each scattergram is a 2D histogram with color representing count density (red = high, yellow = intermediate, green = low, blue = zero). The conductance ranges plotted are (in μS) zero through 146 (g_{Na}), 2.9 (g_{CaT}), 5.4 (g_{CaS}), 134 (g_{KA}), 134 (g_{KCa}), 69 (g_{Kd}) and 0.8 (g_{H}). **(c)** Pairwise scattergrams and histograms for the same 7 conductances as in panel b, showing randomly sampled solution space of models that satisfy target sensor values within 10%. Ranges for each conductance axis

are the same as (b). **(d)** Thinned (5000 points) pairwise scatterplot between g_{Kd} and g_{Na} in converged homeostatic models ('regulated'), and for random sampling ('random'). These scatterplots correspond to the subplots outlined with pink boxes in panels b and c, respectively. Example voltage traces of labeled models are plotted to the right for several different points in the solution space (horizontal line = 0 mV).

Figure 4. Anti-homeostatic regulation can coexist with homeostatic regulation in a complex model (a) Regulation coefficients in the original Liu et al. model (left) and in an alternate version in which regulation coefficients for g_{Ka} are reversed (right). Each coefficient determines whether a conductance is up or down-regulated when sensors are above or below targets (+1 = up-regulate if below target/down-regulate if above target; -1 = down-regulate if below target/up-regulate if above target.) **(b)** Pairwise scattergrams and histograms of the final values for the 7 regulated maximal conductances after one hour simulated time using the original parameters of the Liu model (left) and the alternate model (right). Each scattergram is a 2D histogram with color representing count (red = high, yellow = intermediate, green = low, blue = zero). In both sets of scattergrams the ranges plotted are zero through 440 µS (g_{Na}), 8.6 µS (g_{CaT}), 16.2 µS (g_{CaS}), 402 µS (g_{KA}), 402 µS (g_{KCa}), 207 µS (g_{Kd}), 2.3 µS (g_H) **(c)** Detail of the pairwise relationships between g_{Kd}/g_{Na} and g_H/g_{CaT} (pink boxes in b) shown as thinned scatter plots (5000 points) for the original model (top) and the alternate model (bottom). Example voltage traces of labeled points in solution space are shown to the right (horizontal line = 0 mV).

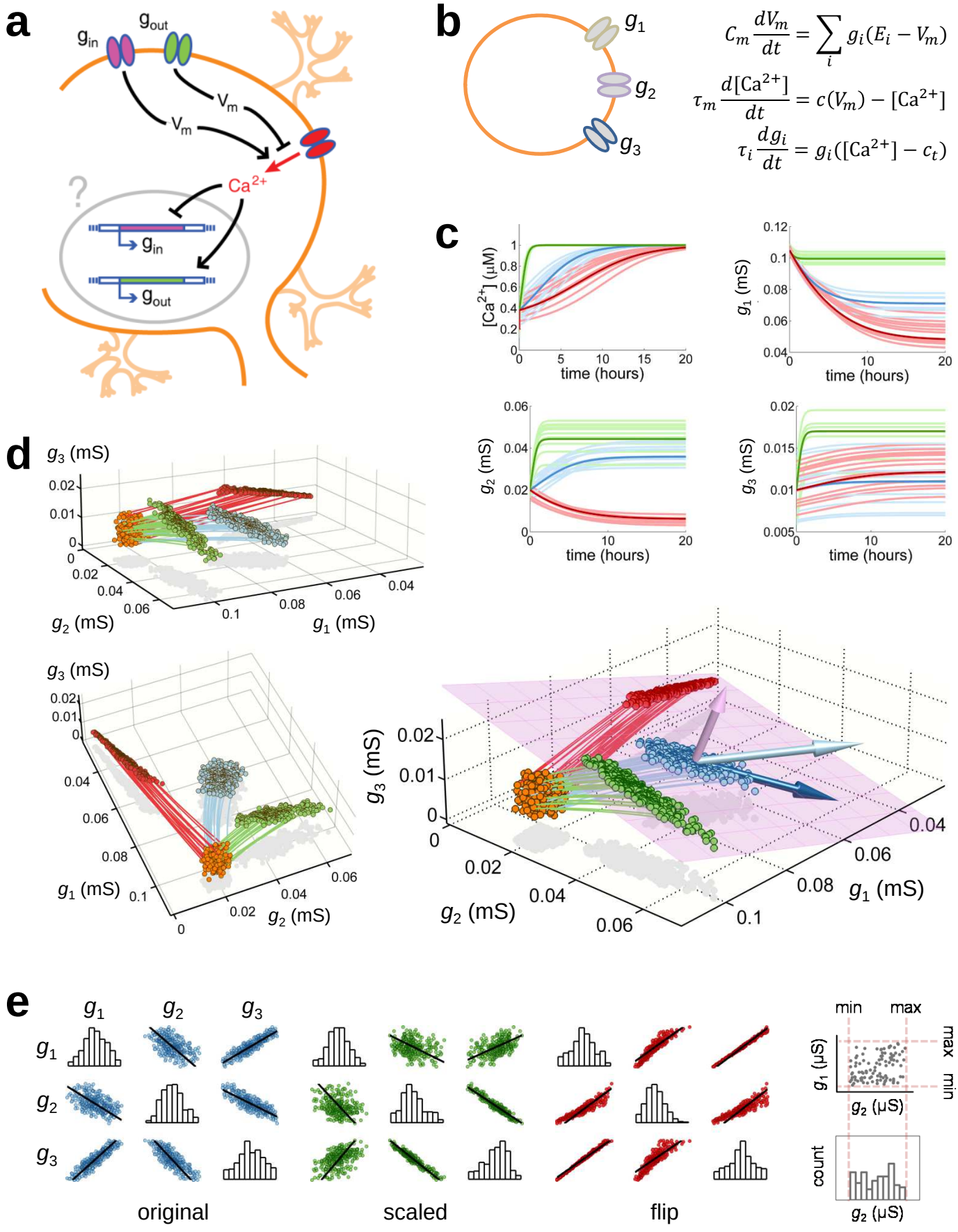
a
b
c
d
e
$C_m \frac{dV_m}{dt} = \sum_i g_i(E_i - V_m)$
$\tau_m \frac{d[Ca^{2+}]}{dt} = c(V_m) - [Ca^{2+}]$
$\tau_i \frac{dg_i}{dt} = g_i([Ca^{2+}] - c_t)$
time (hours)
original
scaled
flip
min
max

Figure 1

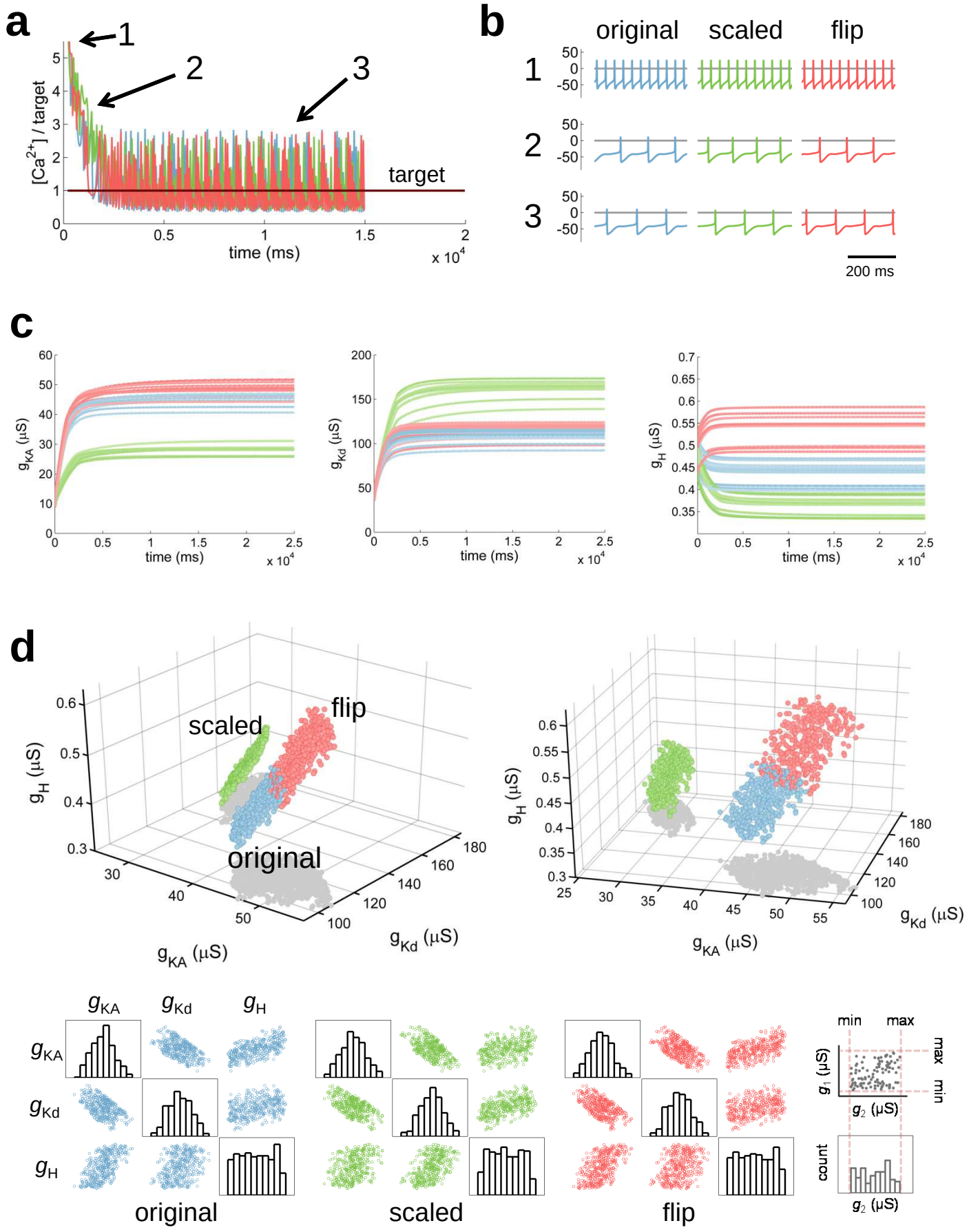
a
1
2
3
[Ca2+] / target
target
time (ms)
x 10^4
b
original
scaled
flip
200 ms
c
gKA (µS)
gKd (µS)
gH (µS)
time (ms)
d
scaled
flip
original
gKA (µS)
gKd (µS)
gH (µS)
min
max

Figure 2

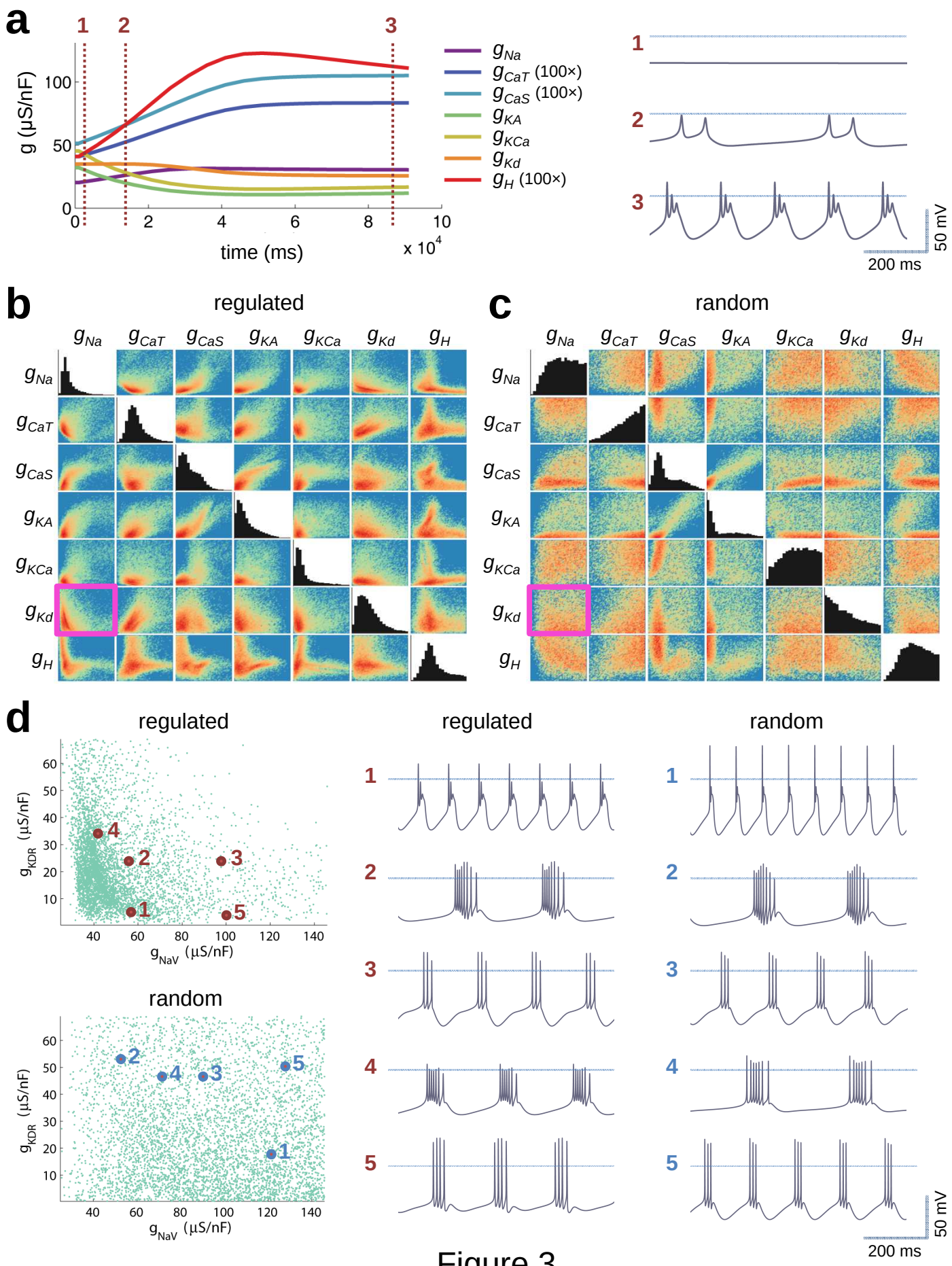
a
1
2
3
g (μS/nF)
100
50
0
0
2
4
6
8
10
x 10^4
time (ms)
g_Na
g_CaT (100×)
g_CaS (100×)
g_KA
g_KCa
g_Kd
g_H (100×)
1
2
3
50 mV
200 ms
b
regulated
c
random
g_Na
g_CaT
g_CaS
g_KA
g_KCa
g_Kd
g_H
d
regulated
random
g_KDR (μS/nF)
g_NaV (μS/nF)
60
50
40
30
20
10
40
60
80
100
120
140
4
2
3
1
5
regulated
random
1
2
3
4
5
50 mV
200 ms

Figure 3

a

original regulation coefficients

	g_{Na}	g_{CaT}	g_{CaS}	g_{KA}	g_{KCa}	g_{Kd}	g_{H}
Fast	1	0	0	0	0	1	0
Slow	0	1	1	-1	-1	-1	1
Mean	0	0	0	-1	-1	0	1

alternate regulation coefficients

	g_{Na}	g_{CaT}	g_{CaS}	g_{KA}	g_{KCa}	g_{Kd}	g_{H}
Fast	1	0	0	0	0	1	0
Slow	0	1	1	1	-1	-1	1
Mean	0	0	0	1	-1	0	1

b

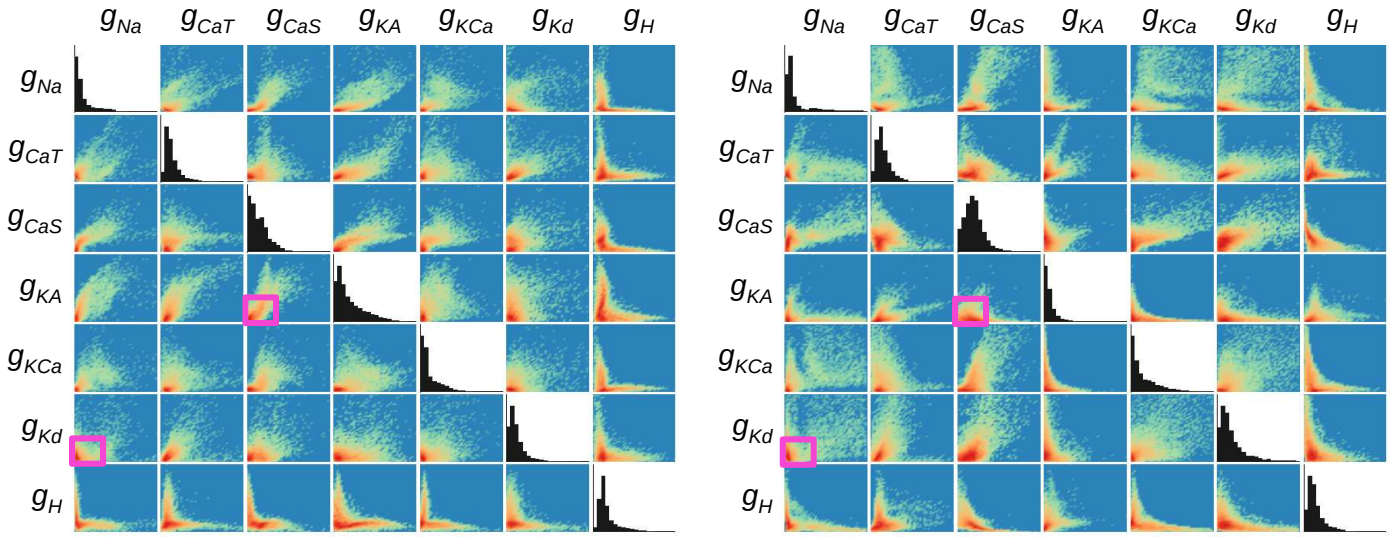

c

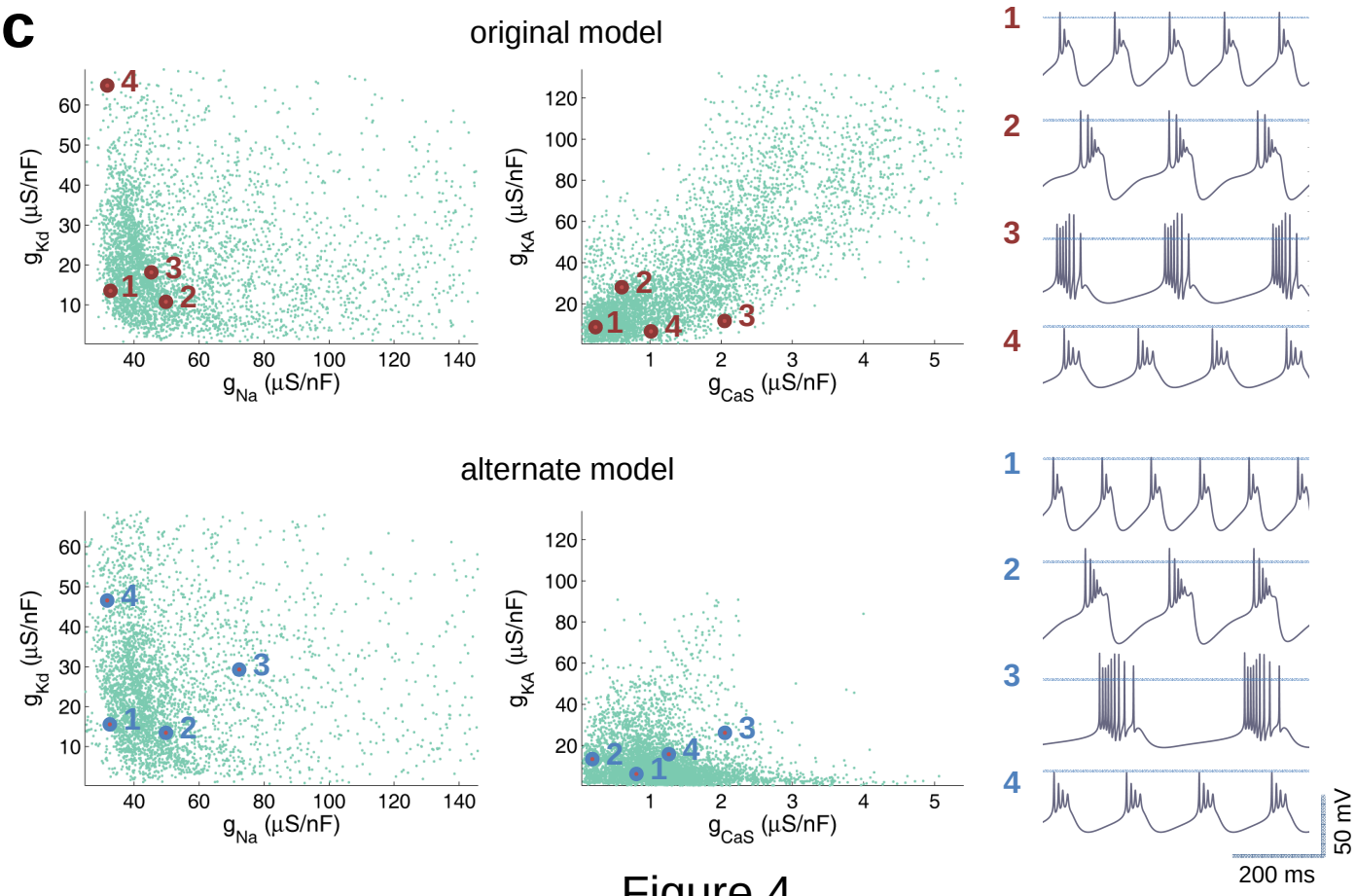

Figure 4